that for the $(0, 0_0)_g$ pair, in accord with the theoretical prediction of a strong curvature coupling of this mode to the reaction coordinate (26–28). To reconcile these seemingly conflicting predictions, the experimental results suggest that the low-frequency bending vibrations of CHD_3, despite its adiabatic correlation to the $(0, 2_1)$ product pair, do not preserve their characters onto the analogous motions of the CD_3 products but rather behave as transitional modes in this reaction by promptly funneling the vibrational energy into the rotational and translational motions of the departing products.

In the stretch-excited reaction, the correlated angular distributions of the two product pairs exhibit very different patterns but bear strong resemblance to the distributions of corresponding product pairs from the ground-state reaction. By pattern comparison, we assert that the $(1, 0_0)_s$ pair is produced adiabatically with the salient forward peak resulting from a resonance state temporarily trapped by the dynamic well of the stretch-excited (red) curve in Fig. 4 (4, 30, 32). In that regard, the observation of a step-like feature in the reactive excitation function near threshold (Fig. 2A) is particularly noteworthy, because a similar feature has been observed experimentally in F + HD and confirmed theoretically as an unambiguous fingerprint for reactive resonance (32–34); this small step also echoes our recent contention for a resonance in the analogous Cl + CH_4 reaction (30).

In contrast, the pattern of the $(0, 0_0)_s$ pair suggests the presence of nonadiabatic pathways induced by the curvature coupling of stretching motions to the reaction coordinate (26–28). Hence, a bifurcation of reaction paths for stretch-excited reactants must occur, presumably near the entrance valley of the transition state. The vibrational branching fraction for the nonadiabatic pathway is quite substantial, $\sigma_s^0/(\sigma_s^0 + \sigma_s^1) \sim 0.55$ from Fig. 3 (where σ_s^0 and σ_s^1 are the integral cross sections for the $(0,0_0)_s$ and $(1,0_0)_s$ product pairs from the stretch-excited reaction, respectively), indicating a facile process. Theory also predicts a strong Coriolis coupling between the stretching and bending modes (20, 27); this facile nonadiabatic transition could then be mediated and facilitated by the transitional nature of the bending motions of the CD_3 moiety during the course of the reaction.

References and Notes

1. J. C. Polanyi, *Acc. Chem. Res.* **5**, 161 (1972).
2. R. N. Zare, *Science* **279**, 1875 (1998).
3. F. F. Crim, *Acc. Chem. Res.* **32**, 877 (1999).
4. K. Liu, *J. Chem. Phys.* **125**, 132307 (2006).
5. K. Liu, *Phys. Chem. Chem. Phys.* **9**, 17 (2007).
6. S. Yoon, S. Henton, A. N. Zivkovic, F. F. Crim, *J. Chem. Phys.* **116**, 10744 (2002).
7. S. Yoon, R. J. Holiday, F. F. Crim, *J. Chem. Phys.* **119**, 4755 (2003).
8. S. Yoon, R. J. Holiday, E. L. Sibert III, F. F. Crim, *J. Chem. Phys.* **119**, 9568 (2003).
9. R. J. Holiday, C. H. Kwon, C. J. Annesley, F. F. Crim, *J. Chem. Phys.* **125**, 133101 (2006).
10. W. R. Simpson, T. P. Rakitzis, S. A. Kandel, T. Lev-On, R. N. Zare, *J. Phys. Chem.* **100**, 7938 (1996).
11. W. R. Simpson, T. P. Rakitzis, S. A. Kandel, A. J. Orr-Ewing, R. N. Zare, *J. Chem. Phys.* **103**, 7313 (1995).
12. S. A. Kandel, R. N. Zare, *J. Chem. Phys.* **109**, 9719 (1998).
13. Z. H. Kim, A. J. Alexander, H. A. Bechtel, R. N. Zare, *J. Chem. Phys.* **115**, 179 (2001).
14. Z. H. Kim, H. A. Bechtel, R. N. Zare, *J. Am. Chem. Soc.* **123**, 12714 (2001).
15. H. A. Bechtel, Z. H. Kim, J. P. Camden, R. N. Zare, *J. Chem. Phys.* **120**, 791 (2004).
16. H. A. Bechtel, J. P. Camden, D. J. A. Brown, R. N. Zare, *J. Chem. Phys.* **120**, 5096 (2004).
17. H. A. Bechtel et al., *Angew. Chem. Int. Ed.* **44**, 2382 (2005).
18. J. Zhou, J. J. Lin, B. Zhang, K. Liu, *J. Phys. Chem. A* **108**, 7832 (2004).
19. S. S. Yan, Y.-T. Wu, K. Liu, *Phys. Chem. Chem. Phys.* **9**, 250 (2007).
20. J. Sanson, J. C. Corchado, C. Rangel, J. Espinosa-Garcia, *J. Phys. Chem. A* **110**, 9568 (2006).
21. J. J. Lin, J. Zhou, W. Shiu, K. Liu, *Rev. Sci. Instrum.* **74**, 2495 (2003).
22. J. J. Lin, J. Zhou, W. Shiu, K. Liu, *Science* **300**, 966 (2003).
23. The innermost ring labeled as $(1, 0_0)_{Cl*}$ arises from ground-state CHD_3 reacting with spin-orbit–excited $Cl(^2P_{1/2})$, the discussion of which is beyond the scope of this report.
24. The rapid decline near threshold in Fig. 2C has an energetic origin and could account for the comparatively larger enhancement factors reported in previous studies of isotopically analogous reactions. In a typical "photoloc" (photoinitiated bimolecular reactions with the use of the law of cosines) experiment (6–16), the reaction of the Cl atom with methane has an average E_c of about 3.5 kcal/mol with a comparable energy spread. Averaging the reactivity ratio shown in Fig. 2C over this energy spread will then yield an enhancement factor that is substantially higher than its actual ratio. Similarly, the $HCl(v' = 1)$ branching fraction from the photoloc experiment will be somewhat smaller because of threshold effects (Fig. 3).
25. One issue may cloud the present comparison: Only $CD_3(v = 0)$ products were probed in this work. Although these results remain a reasonable approximation to total reactivity for the ground-state reaction, the same may not hold for the stretch-excited one. A recent, preliminary investigation of the latter reaction at $E_c = 8.1$ kcal/mol indicated that the two pairs $(0, 0_0)_s$ and $(1, 0_0)_s$ probed in this work account for about two-thirds of the total product distribution, with the remainder distributed among the umbrella-excited CD_3 products. Taking this factor into account, the stretching enhancement factor at 8.1 kcal/mol shown in Fig. 2E will then rise from ~0.95 to 1.4, which is still a rather modest preferential enhancement and almost equivalent to the bending enhancement factor.
26. W. T. Duncan, T. N. Truong, *J. Chem. Phys.* **103**, 9642 (1995).
27. J. C. Corchado, D. G. Truhlar, J. Espinosa-Garcia, *J. Chem. Phys.* **112**, 9375 (2000).
28. J. F. Castillo, F. J. Aoiz, L. Banares, *J. Chem. Phys.* **125**, 124316 (2006).
29. J. Zhou, B. Zhang, J. J. Lin, K. Liu, *Mol. Phys.* **103**, 1757 (2005).
30. B. Zhang, K. Liu, *J. Chem. Phys.* **122**, 101102 (2005).
31. A tiny fraction, ~2% (Fig. 3), does reach the excited stretching curve and gets temporarily trapped in the dynamic well that leads to the $(1, 0_0)_g$ product pair. Its $I(\theta)$-θ-E_c pattern displays both a direct-scattering ridge and sharp forward and backward peaking, characteristic features for a short-lived complex reaction mechanism (4, 30). Thus, the formation of the $(1, 0_0)_g$ pair involves contributions from both pathways.
32. S.-H. Lee, F. Dong, K. Liu, *J. Chem. Phys.* **125**, 133106 (2006).
33. R. T. Skodje et al., *J. Chem. Phys.* **112**, 4536 (2000).
34. R. T. Skodje et al., *Phys. Rev. Lett.* **85**, 1206 (2000).
35. The National Science Council of Taiwan supported this work under grant no. 95-2119-M-001-002.

The Structure of Ferrihydrite, a Nanocrystalline Material

F. Marc Michel,[1,2]* Lars Ehm,[1,2] Sytle M. Antao,[3] Peter L. Lee,[3] Peter J. Chupas,[3] Gang Liu,[1,4] Daniel R. Strongin,[1,4] Martin A. A. Schoonen,[1,2] Brian L. Phillips,[1,2] John B. Parise[1,2,5]

Despite the ubiquity of ferrihydrite in natural sediments and its importance as an industrial sorbent, the nanocrystallinity of this iron oxyhydroxide has hampered accurate structure determination by traditional methods that rely on long-range order. We uncovered the atomic arrangement by real-space modeling of the pair distribution function (PDF) derived from direct Fourier transformation of the total x-ray scattering. The PDF for ferrihydrite synthesized with the use of different routes is consistent with a single phase (hexagonal space group $P6_3mc$; a = ~5.95 angstroms, c = ~9.06 angstroms). In its ideal form, this structure contains 20% tetrahedrally and 80% octahedrally coordinated iron and has a basic structural motif closely related to the Baker-Figgis δ-Keggin cluster. Real-space fitting indicates structural relaxation with decreasing particle size and also suggests that second-order effects such as internal strain, stacking faults, and particle shape contribute to the PDFs.

Ferrihydrite is ubiquitous in many near-surface environments (1, 2) and is routinely used in industrial applications such as direct coal liquefaction and metallurgical processing (3, 4). It occurs in pristine soils and sediments as the precursor to hematite and often in areas contaminated by acid mine drainage (5). Because of its extremely high surface area and reactivity, ferrihydrite plays a substantial role in the sequestration of contaminants from groundwater and streams through adsorption and co-precipitation. As such, it is also manufactured for use as a scavenger of heavy metals and metalloids during the treatment of wastewaters and in remedial activities. It is also suspected to form the inorganic core of ferritin, an iron storage protein that plays a key role in controlling the levels of iron in plants, animals, and microbes (6).

Even with the considerable attention given to the chemical and physical properties of ferrihydrite in previous research, there is no consensus on the crystal structure of this mineral. The primary impediment to the development of a definitive structural determination is the size of individual ferrihydrite crystallites, which are typically <10 nm (nanocrystalline). With regard to structure, most of the disagreement centers on the possible presence of multiple structural phases and the local environment of iron (7–10) and has implications for understanding its reactivity, magnetic properties, and overall chemical composition. No single formula is widely accepted for ferrihydrite; this is attributed to variable water content and a lack of a known crystal structure (11). Ferrihydrite is commonly designated as "two-line" or "six-line" on the basis of the number of poorly defined, broadened maxima observed in x-ray diffraction (XRD) patterns. Determining a starting structural model for this phase is particularly challenging because ferrihydrite has no known well-crystalline counterpart that can be synthesized in the laboratory or found in nature. We have recently shown that the short- and intermediate-range ordering in synthetic nanocrystalline ferrihydrite is consistent for scattering domain sizes ranging from 2 to 6 nm, and therefore the structure of ferrihydrite appears to be single phase (12). This result contradicts some previous studies (7–10) and is fundamentally different from the current multiphase structure model that is increasingly cited for this phase.

Synthetic ferrihydrite with three distinct average coherent scattering domain sizes of approximately 2 (Fhyd2), 3 (Fhyd3), and 6 nm (Fhyd6) were synthesized and evaluated as part of this study [see supporting online material (SOM) text]. We used the PDF method to perform a structural analysis, which involved a comparison between PDFs generated from the experimental scattering data and those calculated from structural models [see (13) for a review]. A highly constrained "Rietveld-like" refinement can be performed on a properly normalized PDF, $G(r)$, in which the unit cell dimensions, atomic positions, displacement, occupancies, and other model-dependent parameters are varied to improve the fit between the observed and calculated PDF (14). The starting model best describing the distribution of interatomic distances in ferrihydrite is isostructural to the mineral akdalaite ($Al_{10}O_{14}(OH)_2$) (SOM text) (15) and was identified by using the few positions of the most identifiable Bragg features in the XRD patterns.

On the basis of the real-space fitting results, we contend that the structure of ferrihydrite with domain sizes ranging from 2 to 6 nm can be adequately described by a single-phase model with the hexagonal space group $P6_3mc$ and a unit cell with average dimensions of $a = {\sim}5.95$ Å and $c = {\sim}9.06$ Å (Fig. 1). On the basis of this structure in its ideal form, the chemical formula for ferrihydrite is $Fe_{10}O_{14}(OH)_2$. Thermal analysis strongly suggests the presence and particle-size dependence of additional surface-bound water (12). Although the structure of ferrihydrite can be satisfactorily described by a periodic model (Fig. 2), residuals in the fitting results suggest that second-order effects such as disorder, surface relaxation, internal strain, defects (e.g., stacking faults), particle shape (16), and/or interparticle correlations may also contribute to the experimental PDFs. Misfits in the region between 2.5 and ~6 Å (Fig. 2) are reminiscent of those found in a similar study of γ-Al_2O_3, in which differences were attributed to nanometer-sized domains (~1 nm) reflecting stacking faults in the matrix (17).

The basic structural motif of the model, which is closely related to the Baker-Figgis δ-Keggin cluster (18), consists of 13 iron atoms and 40 oxygens (Fig. 3). The central tetrahedrally coordinated Fe is connected by μ_4-oxo bridges to 12 peripheral octahedrally coordinated Fe atoms arranged in edge-sharing groups of three. The 2- to 6-nm ferrihydrite nanoparticles can then be described as a three-dimensional packing of these clusters with adjacent clusters connected by a common pair of edge-shared octahedra, forming μ_4-oxo bridges from the three μ_2-OH groups cis to each of the μ_4-oxo centers in the bare cluster. This arrangement creates a cubane-like moiety corresponding to four edge-shared Fe octahedra (Fig. 1). Fitting results indicate that some param-
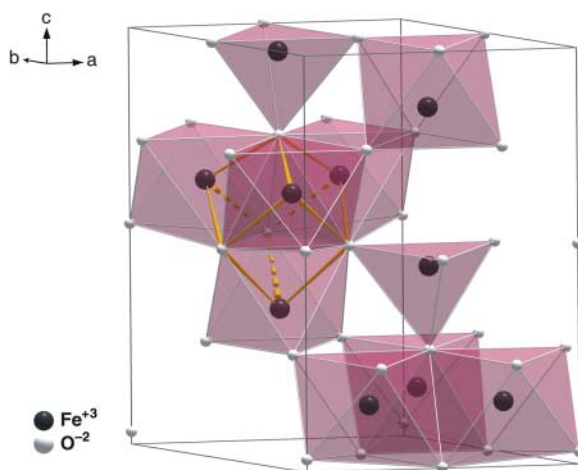
Fig. 1. Polyhedral representation of the hexagonal unit cell for ferrihydrite. The bonded atoms (yellow) define a cubane-like moiety that connects the basic structural motif of the model.

Fig. 2. The PDF, also known as $G(r)$, for Fhyd6 (**A**), Fhyd3 (**B**), and Fhyd2 (**C**) plotted to 20 Å (gray x's, which form a gray line when close together) with the refined fit of the model overlaid (solid black) for each. Difference plots are shown immediately below.
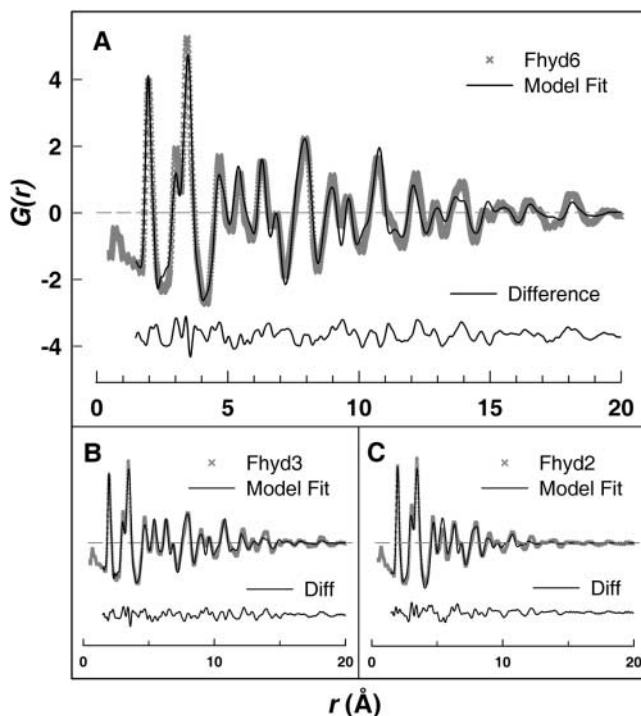
[1]Center for Environmental Molecular Science (CEMS), Stony Brook University, Stony Brook, NY 11794, USA. [2]Department of Geosciences, Stony Brook University, Stony Brook, NY 11794, USA. [3]Advanced Photon Source, Argonne National Laboratory, Argonne, IL 60439, USA. [4]Department of Chemistry, Temple University, Philadelphia, PA 19122, USA. [5]Department of Chemistry, Stony Brook University, Stony Brook, NY 11794, USA.

*To whom correspondence should be addressed. E-mail: fmichel@ic.sunysb.edu

eters such as unit cell dimensions and occupancies change systematically as the average domain size decreases from 6 to 2 nm for Fhyd6 and Fhyd2, respectively. Additionally, the degree of distortion of the Fe1 polyhedra varies as indicated in part by the change in the refined z parameter for the O1 site, but despite these differences, the cluster-like structural motif remains. Such changes could reflect the occurrence of stacking defects or internal strain in the structure but are not fully understood.

This structure in its ideal form consists of 20% FeO_4 and 80% FeO_6 polyhedra. However, the Fe2 and Fe3 sites show a decrease in occupancy with decreasing particle size, whereas no particle size–dependent changes are observed for the fully occupied Fe1 site. This trend might reflect an overall increase in disorder resulting from the change in ratio of Fe atoms near the surface versus interior with decreasing particle size (19). These surface regions of ferrihydrite are anticipated to be predominantly octahedrally coordinated given the overall topology of the structure presented and the unlikely existence of coordinatively unsaturated Fe at the hydrated surfaces. The refined parameters for each sample are available in the SOM text.

The presence of tetrahedrally coordinated iron in ferrihydrite has been the subject of considerable debate. Previous estimates based on a variety of techniques have ranged from 0 to ~40%, approximately the same amount found in maghemite (γ-Fe_2O_3), and even up to 100% (20–22). In a recent study using electron energy loss spectroscopy (EELS) to evaluate the effects of electron beam damage to ferrihydrite, Pan et al. (23) observed the reduction of Fe^{3+} to Fe^{2+} and a migration of Fe from octahedral to tetrahedral sites with increasing electron dose. These results highlight how investigations carried out under the high vacuum of the transmission electron microscope may cause substantial, and perhaps undetected, changes to occur in a sample. Such changes must now be considered when evaluating the most current and increasingly cited multiphase model for ferrihydrite that was purportedly confirmed using electron nanodiffraction (7, 8).

Pan et al. estimated, by linear extrapolation to very low electron dose (1 electron nm^{-2}), that tetrahedrally coordinated Fe^{3+} could be absent from the pristine structure of ferrihydrite and may appear only as a result of electron beam damage. However, this is a minimum estimate. Peak fitting of the energy-loss spectrum recorded at the lowest measured electron dose (3×10^4 electron nm^{-2}) indicates that, at this dose, as much as $25 \pm 15\%$ (where 15% is the experimental error) of the total iron in the mineral is tetrahedrally coordinated Fe^{3+} (24). Mössbauer studies performed at temperatures as low as 4.2 K by our group and others (25) show spectra completely split magnetically and appearing as sextets. Although this behavior does not rule out the existence of discretely different iron sites, the existence of 4-coordinated iron remains inconclusive (26). Future Mössbauer studies at subliquid He temperatures may prove useful for further resolving this debate, as was demonstrated in a study of a compound containing a structurally related Fe_{13} cluster (($C_5H_6N^+$)$_5$[$Fe_{13}F_{24}(OCH_3)_{12}O_4$]· CH_3OH·$4H_2O$) (27).

Whether a 2-nm (i.e., ~30 unit cells) or even a 6-nm platelike particle can be described by a periodic model is debatable. Perhaps a particle with maximum dimensions of only several nanometers and possessing substantial disorder might better be described by a single large ensemble of atoms. We found that the satisfactory fit obtained by the single-phase defect-free unit cell for ferrihydrite in this study does not support this view. Synthetic ferrihydrite samples with average coherent scattering domain sizes ranging from 2 to 6 nm can be described by a single-phase periodic structure that does not require multiphase, size-dependent models (fig. S1 and SOM text). The proposed structure model for ferrihydrite does not address the positions for H sites. However, we anticipate that, with the iron and oxygen framework established, neutron total scattering studies on deuterated ferrihydrite will provide a complete model.

Quantitatively evaluating the structures of materials that exhibit coherent periodicity only on length scales on the order of <10 nm and that

are sensitive to changes under vacuum represents a considerable challenge for conventional diffraction methods and electron imaging techniques. Although ab initio structure determination of nanocrystalline materials is in its infancy (28), domain-limited PDFs from total scattering data to very high reciprocal space values (i.e., $\geq$25 Å^{-1}) provide a map of interatomic distances, which can be fitted with competing structure models (29). Such models may appear to be quite similar in terms of short-range ordering (i.e., distances of 1 to 5 Å) but are distinguishable over intermediate-range length scales (i.e., 5 to 20 Å) because of differences in overall topology. Although it is not possible to demonstrate the uniqueness of a successful model, a solution consistent with the experimental PDF over 20 Å, or more, allows for strong confidence in the result. Traditional structure solution in well-ordered periodic materials relies on the interpretation of sharp Bragg reflections to derive an initial unit cell. This conventional approach is generally not feasible for nanocrystalline materials like ferrihydrite because of the lack of discernable Bragg reflections in diffraction patterns dominated by broad diffuse scattering. This diffuse component results not only from extremely small coherent scattering domain sizes but also from surface relaxation, strain, and complex disorder that often distinguish the structures of nanocrystalline materials from their bulk counterparts (30). Thus, the interpretation of the broad diffuse diffraction patterns of nanometer-sized crystals through observation of structural details in real space by means of the PDF method currently provides the best means of discrimination between existing, and potentially closely related, models.

References and Notes
1. D. G. Rancourt et al., Am. Mineral. **86**, 834 (2001).
2. U. Schwertmann, L. Carlson, E. Murad, Clays Clay Miner. **35**, 297 (1987).
3. G. P. Huffman et al., Energy Fuels **7**, 285 (1993).
4. P. A. Riveros, J. E. Dutrizac, P. Spencer, Can. Metall. Q. **40**, 395 (2001).
5. R. M. Cornell, U. Schwertmann, The Iron Oxides: Structure, Properties, Reactions, Occurrence and Uses (VCH, Weinheim, Germany, 1996).
6. A. Lewin, G. R. Moore, N. E. Le Brun, Dalton Trans. **2005**, 3597 (2005).
7. V. A. Drits, B. A. Sakharov, A. L. Salyn, A. Manceau, Clay Miner. **28**, 185 (1993).
8. D. E. Janney, J. M. Cowley, P. R. Buseck, Am. Mineral. **85**, 1180 (2000).
9. D. E. Janney, J. M. Cowley, P. R. Buseck, Am. Mineral. **86**, 327 (2001).
10. E. Jansen, A. Kyek, W. Schafer, U. Schwertmann, Appl. Phys. Mater. Sci. Process. **74**, S1004 (2002).
11. J. L. Jambor, J. E. Dutrizac, Chem. Rev. **98**, 2549 (1998).
12. F. M. Michel et al., Chem. Mater. **19**, 1489 (2007).
13. S. J. L. Billinge, M. G. Kanatzidis, Chem. Commun. **7**, 749 (2004).
14. T. Egami, S. J. L. Billinge, Underneath the Bragg Peaks: Structural Analysis of Complex Materials, vol. 7 of Pergamon Materials Series, R. W. Cahn, Ed. (Elsevier, Oxford, 2003).
15. S. L. Hwang, P. Y. Shen, H. T. Chu, T. F. Yui, Int. Geol. Rev. **48**, 754 (2006).
16. K. Kodama, S. Iikubo, T. Taguchi, S. Shamoto, Acta Crystallogr. A **62**, 444 (2006).

Fig. 3. Polyhedral representation of the ideal ferrihydrite structure viewed along the c axis. The central FeO_4 tetrahedra are surrounded by 12 FeO_6 octahedra.
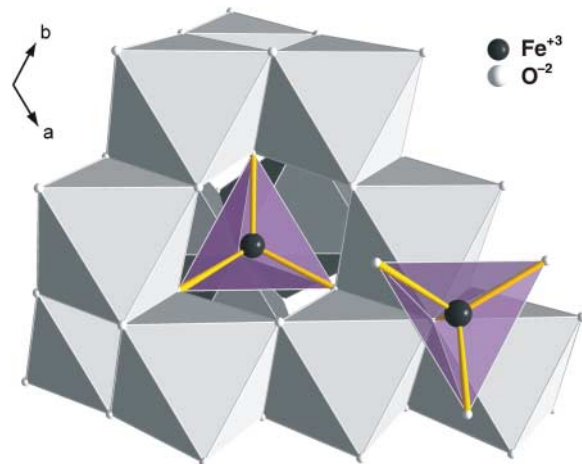
17. G. Paglia, E. S. Bozin, S. J. L. Billinge, *Chem. Mater.* **18**, 3242 (2006).
18. W. H. Casey, *Chem. Rev.* **106**, 1 (2006).
19. I. Joumard *et al.*, *Phys. Rev. B* **74**, 205411 (2006).
20. G. W. Brady *et al.*, *Biochemistry* **7**, 2185 (1968).
21. R. A. Eggleton, R. W. Fitzpatrick, *Clays Clay Miner.* **36**, 111 (1988).
22. Q. A. Pankhurst, R. J. Pollard, *Clays Clay Miner.* **40**, 268 (1992).
23. Y. Pan *et al.*, *Micron* **37**, 403 (2006).
24. Y. Pan, Ph.D. thesis, University of Leeds, Leeds, UK (2007).
25. Y. Guyodo *et al.*, *Physics of the Earth and Planetary Interiors* **154**, 222 (2006).
26. E. Murad, U. Schwertmann, *Am. Mineral.* **65**, 1044 (1980).
27. J. van Slageren *et al.*, *Phys. Rev. B* **73**, 014422 (2006).
28. P. Juhas, D. M. Cherba, P. M. Duxbury, W. F. Punch, S. J. L. Billinge, *Nature* **440**, 655 (2006).
29. V. Petkov *et al.*, *Phys. Rev. B* **65**, 092105 (2002).
30. B. Gilbert, F. Huang, H. Z. Zhang, G. A. Waychunas, J. F. Banfield, *Science* **305**, 651 (2004).
31. This work is dedicated in memoriam to Charles E. McClennen, Professor of Geology, Colgate University. Support provided by the Center for Environmental Molecular Science (CEMS); NSF Awards CHE0221934, DMR-045244, and EAR-0510501; the U.S. Department of Education through the Graduate Assistance in Areas of National Need Program Sponsor identification P200A060248; and the U.S. Department of Energy, Basic Energy Sciences grant no. DE-FG02-03ER-47085. Data collection was performed at X-Ray Operation and Research beamline 11-ID-B at the Advance Photon Source, Argonne National Laboratory, and use is supported by the U.S. Department of Energy, Office of Science, Office of Basic Energy Sciences, under contract no. DE-AC02-06CH11357. We thank D. Dyar for her efforts in the collection of Mössbauer data on these samples.

Deformation of (Mg,Fe)SiO₃ Post-Perovskite and D″ Anisotropy

Sébastien Merkel,[1,2]* Allen K. McNamara,[3] Atsushi Kubo,[4]† Sergio Speziale,[1]‡ Lowell Miyagi,[1] Yue Meng,[5] Thomas S. Duffy,[4] Hans-Rudolf Wenk[1]

Polycrystalline $(Mg_{0.9},Fe_{0.1})SiO_3$ post-perovskite was plastically deformed in the diamond anvil cell between 145 and 157 gigapascals. The lattice-preferred orientations obtained in the sample suggest that slip on planes near (100) and (110) dominate plastic deformation under these conditions. Assuming similar behavior at lower mantle conditions, we simulated plastic strains and the contribution of post-perovskite to anisotropy in the D″ region at the Earth core-mantle boundary using numerical convection and viscoplastic polycrystal plasticity models. We find a significant depth dependence of the anisotropy that only develops near and beyond the turning point of a downwelling slab. Our calculated anisotropies are strongly dependent on the choice of elastic moduli and remain hard to reconcile with seismic observations.

Seismological observations of the lowermost mantle (the D″ region) have revealed a region of great complexity distinct from the overlying deep mantle (*1, 2*). Unlike the bulk of the lower mantle, the core-mantle boundary (CMB) includes large-scale regions with apparent seismic anisotropy (*3*). It has been suggested that this anisotropy could reflect lattice-preferred orientation (LPO) of minerals (*4*) or alignment of structural elements, including layers of melt (*5, 6*). A number of lines of evidence now suggest that the transition from a perovskite (Pv) to a post-perovskite (pPv) phase in (Mg,Fe)SiO₃ (*7, 8*) could explain important properties of D″ (*9–13*). However, the influence of this phase transition on our understanding of D″ anisotropy remains ambiguous. In this paper, we present multiscale modeling of deformation-induced anisotropy from (Mg,Fe)SiO₃-pPv in D″. This work is a combination of high-pressure deformation experiments on (Mg,Fe)SiO₃-pPv and numerical modeling of convection using polycrystal plasticity to predict strain and anisotropy in D″.

We deformed a sample of polycrystalline $(Mg_{0.9},Fe_{0.1})SiO_3$-pPv plastically in the diamond anvil cell in compression between 145 and 157 GPa and observed the evolution of LPO in situ using angle dispersive radial x-ray diffraction (fig. S1) at the High-Pressure Collaborative Access Team (HPCAT) of the Advanced Photon Source (beamline 16-ID-B). Starting material was a powder of natural orthopyroxene (*14*) mixed with 10 weight percent Pt powder that served as a laser absorber. The sample was initially compressed to high pressure, at which we could not observe coherent diffraction from within the sample, and then converted into the pPv phase by laser heating at different sample positions at a temperature of 1700 K for 20 min and 2000 K for ~15 min. After the phase transformation, pressure and differential stress in the sample were 145 and 7.2 GPa, respectively. They were then increased in two steps to 157 and 8.5 GPa over the course of 30 hours. At every step, we collected radial diffraction patterns to evaluate the pressure, stress, and LPO in the sample (*14*) (table S1).

The diffraction images show substantial variations of diffraction peak positions and intensities with orientation relative to the compression direction that can be used to estimate stress and deduce LPO (*14*) (Fig. 1). For instance, we observed that the diffraction intensity in the compression direction is minimal for 004 and 022, whereas it is maximal for 113 and 132. The texture we obtain (*14*) is represented in Fig. 2. In contrast with low-temperature and lower-pressure observations on the Mn₂O₃ (*15*) and CaIrO₃ (*16*) pPv analogs, we observed LPO compatible with previous observations on a MgGeO₃-pPv analog deformed under similar conditions (*17*) with a clear minimum at (010) and (001). Those LPO are formed immediately upon synthesizing and heating (Mg,Fe)SiO₃-pPv at high pressure. Minima observed at (010) and (001) preclude slip on (001) and (010) planes, and a comparison of observed textures and results from viscoplastic self-consistent (VPSC) polycrystal plasticity simulations (*18*) indicate that the deformation is likely dominated by slip on planes such as (100) or (110), in agreement with results of first-principles modeling of stacking fault energetics and shear elastic constants SiO₃ (*19*) but in disagreement with first-principles modeling of dislocation cores based on the Peierls model that suggest [001](010) as the easiest slip system (*20*).

There are limitations in our experiment: time scale, grain size, strain, temperature, and deviatoric stresses are quite different from those in D″. Moreover, LPOs are formed immediately upon synthesizing and heating the pPv phase and do not evolve greatly upon further compression. However, assuming that (100) and (110) slip also applies to (Mg,Fe)SiO₃-pPv under deep mantle conditions, we simulated the development of LPO in (Mg,Fe)SiO₃-pPv in D″ combining geodynamic information about macroscopic deformation and the microscopic deformation mechanisms found in the experiment (table S2). Deformation in D″ can be quite complex because it is coupled to larger-scale mantle-wide convective processes. Therefore, we performed our modeling using the entire mantle domain. We used the numerical convection code Citcom (*21*) with the addition of Lagrangian tracers to obtain a proper estimation of the deformational characteristics of

[1]Department of Earth and Planetary Science, University of California, Berkeley, CA 94720, USA. [2]Laboratoire de Structure et Propriétés de l'Etat Solide, UMR CNRS 8008, Université des Sciences et Technologies de Lille, 59655 Villeneuve d'Ascq, France. [3]School of Earth and Space Exploration, Arizona State University, Box 871404, Tempe, AZ 85287–1404, USA. [4]Department of Geosciences, Princeton University, Princeton, NJ 08544, USA. [5]High-Pressure Collaborative Access Team, Carnegie Institution of Washington, Argonne, IL 60439, USA.

*To whom correspondence should be addressed. E-mail: sebastien.merkel@univ-lille1.fr
†Present address: Consortium for Advanced Radiation Sources, University of Chicago, Argonne, IL 60439, USA.
‡Present address: GeoForschungsZentrum Potsdam, Division 4.1, Telegrafenberg, 9-14482 Potsdam, Germany.